TITLE: Smart wing rotation and trailing-edge vortices enable high frequency mosquito flight

AUTHORS: Richard J. Bomphrey, Toshiyuki Nakata, Nathan Phillips, Simon M. Walker

JOURNAL TITLE: Nature

PUBLISHER: Nature Publishing Group

PUBLICATION DATE: 5 April 2017 (online)

DOI: 10.1038/nature21727

Smart wing rotation and trailing-edge vortices enable high frequency mosquito flight

Richard J. Bomphrey[1*], Toshiyuki Nakata[1,2], Nathan Phillips[1], Simon M. Walker[3]

[1]Structure and Motion Laboratory, Royal Veterinary College, University of London, Hatfield, AL9 7TA. United Kingdom.

[2]Graduate School of Engineering, Chiba University, 1-33, Yayoi-cho, Inage-ku, Chiba-shi, Chiba 263-8522 Japan.

[3]Department of Zoology, University of Oxford, South Parks Road, Oxford, OX1 3PS.

*Correspondence to: rbomphrey@rvc.ac.uk

Summary

Mosquitoes exhibit unique wing kinematics; their long, slender wings flap at remarkably high frequencies for their size (>800 Hz) and with lower stroke amplitudes than any other insect group[1]. This shifts weight support away from the translation-dominated, aerodynamic mechanisms used by most insects[2], as well as by helicopters and aeroplanes, towards poorly understood rotational mechanisms that occur when pitching at the end of each half-stroke. Here we report wing kinematics and solve the full Navier-Stokes equations using computational

fluid dynamics with overset grids and validate our results with *in vivo* flow measurements. We show that, while familiar separated flow patterns are used by mosquitoes, much of the aerodynamic force that supports their weight is generated in a manner unlike any previously described flying animal. In total, there are three key features: leading-edge vortices (a well-known mechanism that appears to be almost ubiquitous in insect flight), trailing-edge vortices caused by a novel form of wake capture at stroke reversal, and rotational drag. The two new elements are largely independent of the wing velocity, instead relying on rapid changes in the pitch angle (wing rotation) at the end of each half stroke, and are therefore relatively immune to the shallow flapping amplitude. Moreover, these mechanisms are particularly well-suited to high-aspect ratio mosquito wings.

31 Main Text

32 Mosquitoes disperse, find mates, lay eggs and seek hosts on the wing but their small size and
33 exceedingly high wing beat frequencies present a substantial challenge for biomechanical
34 measurements. To test our prediction that mosquitoes shift lift generation away from the
35 translational phase of the wingbeat and rely more heavily on the pitching rotation phases at the
36 end of each half stroke (Fig. 1), we measured the wing motion and simulated the resulting
37 aerodynamics of the southern house mosquito (*Culex quinquefasciatus,* Say; Supplementary
38 Video*)*. We confirm that mosquitoes have a diminished reliance on leading-edge vortices, an
39 aerodynamic phenomenon that augments lift forces for insects[3-8], birds[9,10] and bats[11] during
40 wing translation. The effect of leading edge vortices is to generate sufficient lift with smaller
41 wings; a clear advantage for flying taxa. Instead, we observed lift enhancement via two
42 mechanisms that are exclusive to mosquitoes thus far; i) lift enhancement due to a trailing-edge
43 vortex captured during stroke reversal and ii) partial weight support due to a newly-described
44 rotational effect at the end of each half stroke. The latter mechanism, rotational drag, has been
45 postulated previously[12,13] but, here, is mediated by exquisitely-timed kinematic patterns that
46 cause a leading-to-trailing edge shift of the pitching axis during stroke reversal.

47 Our analysis of the free-flight kinematics of male *Culex* mosquitoes (Fig. 1A-C) revealed that
48 they flapped their wings at frequencies of 717 ± 59 (mean ± one s.d.) Hz and with amplitudes of
49 just 39°±4°, which is by far the smallest amplitude yet measured for any hovering animal,
50 despite operating at similar scales to fruit flies (Fig. 1D). The stereotypically low amplitudes we
51 measured mean that the 75% radial position of the wing travels just two chord lengths between

stroke reversals. This, in turn, causes substantial aerodynamic consequences and the breakdown of the fluid mechanics assumption that wings act like sweeping helicopter blades[14].

Our simulations of forces, torques, power expenditure and flow fields show great consistency, with the aerodynamic features being entirely robust to the wide variety of body velocities and wing kinematics within the behavioural repertoire we measured (Extended Data Figure 1). We re-validated the CFD solver using particle image velocimetry and the corresponding flow fields matched both qualitatively and quantitatively (Fig. 2).

The three distinct aerodynamic mechanisms occur sequentially during the stoke cycle, each used on both the downstroke and the upstroke: the trailing-edge vortex due to wake capture, the leading-edge vortex, and rotational drag. We present one mosquito by way of example (M08; Fig. 1), although every mosquito we measured exhibited each of these aerodynamic mechanisms (Extended Data Figures 2-6). Five key instants, marked *t1-t5*, are highlighted on the aerodynamic force traces (Fig. 3A). The first key instant (*t1*) corresponds to a peak in lift force early in the downstroke, shortly after pronation, (Fig. 3A, *t1*) due to a strong trailing-edge vortex bound to the hind portion of the wing (Fig. 3F). The trailing-edge vortex forms as the high-velocity induced flow from the preceding upstroke separates as it encounters the trailing edge at a higher angle of attack than in other insects (Extended Data Figure 7). The trailing edge has very low ground speed at this moment but, under the influence of the upstroke wake, the airspeed and pressure gradient are sufficient for the shear layer to roll up into a coherent attached vortex. As it does so, a region of intense negative pressure forms that contributes to weight support.

The trailing-edge vortex is a form of wake capture as it is dependent on flow induced during the previous half stroke. However, it is fundamentally distinct from previously described wake capture effects because a wake structure forms as the flow first encounters the trailing edge of the wing. This contrasts with the simpler case of augmentation or reorientation of lift generated by a forward translating wing. The resultant flow pattern is strikingly reminiscent of the leading-edge vortex pattern seen previously, but it is reversed. Instead, the flow separates at the trailing edge, with streamlines reattaching further forwards along the wing chord, enveloping a coherent attached vortex (Fig. 3F, *t1*). It is also distinct from previous descriptions of a starting vortex (sometimes referred to as a trailing-edge vortex) because it is both bound to the wing surface, rather than left in the wake, and makes a positive contribution to weight support. This transient trailing-edge vortex is quickly shed into the wake as the wing accelerates into the short translational phase, giving way to a leading-edge vortex (Fig. 3G) and a corresponding second peak in lift (Fig. 3, *t2*).

A third peak in lift occurs due to rapid supination during the onset of stroke reversal at the end of the downstroke (Fig. 3, *t3*). The mechanism for this is the recently-described phenomenon of rotational drag [12]. The wing rotates initially around an axis close to the leading edge, resulting in strong forces normal to the posterior wing surface. The signature of this effect is an intense negative pressure appears, again, in the region of the trailing edge. We can differentiate between lift due to rotational drag[12,13] and rotational lift[15,16] because the aerodynamic force vector is normal to the wing surface despite negligible translational velocity of the wing. As the wing decelerates (t/T=0.5), rotational drag makes a reduced contribution to weight support,

94 becoming zero on the point of stroke reversal and even making a small negative impact in some
95 cases (Extended Data Figure 8).

96 On the upstroke, the wing is inverted and the processes are repeated. As such, the fourth key
97 instant (*t4*) corresponds to a new trailing-edge vortex (Fig. 3I) that quickly gives way to another
98 leading-edge vortex (Fig. 3J). The peak in lift force during the late upstroke (*t5*) is a combination
99 of the leading-edge vortex influence as the wing translates, and also rotational drag, because
100 wing rotation begins earlier in the upstroke than downstroke (Fig. 1C). The mechanisms are
101 additive and it is striking that peak force generation happens this late in the wing beat cycle.
102 This contrasts with most other animals, with the exception of fruit flies[17,18], which exhibit
103 maximal forces during the downstroke. High upstroke loads for mosquitoes will have
104 consequences for the mechanical stresses on the wing, which may in turn predicate differences
105 in anatomical architecture such as wing camber or vein cross-section profiles.

106 Quasi-steady modeling has been an important tool for aerodynamicists but it cannot
107 encapsulate wake capture, rotational drag and non-linear vortex phenomena. We produced a
108 quasi-steady model which used dynamic force coefficients based on lift and drag polars at four
109 Reynolds numbers (Extended Data Figure 9) to highlight which wing stroke forces are the result
110 of unconventional mechanisms and will consequently be explained poorly by a quasi-steady
111 model. As expected, the key instants described above–where extra lift is generated through
112 rotational mechanisms–revealed a marked underestimate of the lift calculated from CFD
113 simulations, with a further discrepancy noted as the lift due to rotational drag becomes
114 negative at supination (Fig. 3B). To investigate further the relative importance of aerodynamic
115 phenomena at wing rotation, we simulated the flow fields generated by larger amplitude wing

strokes while maintaining the mean wing tip speed using CFD. This process shifts the balance of force generation back towards conventional, translational aerodynamics and diminishes the relative contribution of the rotational phases. The effect is demonstrated clearly by the increasing discrepancy at instances *t1*, *t3* and *t5* (Fig. 3E).

Leading-edge vortices on the up- and downstrokes produce large regions of negative pressure close to the leading edge of the wing (Fig. 3G,J); however, these are interleaved with trailing-edge vortices and rotational drag effects that principally act on the posterior region, leading to chord-wise fluctuations in the centre of pressure. The key instants *t1* (trailing-edge vortex), *t3* (rotational drag) and *t4* (upstroke trailing-edge vortex) show the dominance of the trailing portion of the wing in lift support, whereas *t2* (the downstroke leading-edge vortex) shows the leading edge as dominant. In the case of *t5*, the leading-edge vortex during the upstroke has grown large enough to encroach into the aft portion of the wing and rotational drag is beginning to take effect so the differential is negligible. Consequently, the wing undergoes fluctuations in the pitching torque, with the location of the centre of pressure sometimes acting in concert with the pitching of wing (Fig. 3C; e.g. *t1* and *t4*), resulting in a low power requirement that suggests passive pitching through aeroelastic effects (Fig. 3D).

Crucial to the mosquito's ability to generate forces large enough to support its weight in flight is the high angular rate and exquisite timing of stroke reversal. Lift due to rotational drag is proportional to the square of the pitching angular rate, but equally important is the precise axis of rotation. In mosquitoes, the pitching rotational axis of the wing moves from leading to trailing edge during pronation at the end of the upstroke (Fig. 4A). By rotating first around an axis close to the leading edge, low pressure develops close to the trailing edge, creating a

component of aerodynamic force that supports the mosquito's weight and drawing the leading-edge vortex towards the trailing edge. If this rotational axis were maintained throughout pronation, the lift due to rotational drag would become negative as the wing angle passed through vertical. However, by shifting the axis of rotation progressively towards the trailing edge as the wing rotates, the new aerodynamic upper surface of the wing develops a region of negative pressure close to the leading edge. This region contributes positively to weight support through rotational drag at the start of the new half stroke but also initiates flow separation for the new leading-edge vortex to form and grow during the downstroke (*t2*). At the end of the downstroke, the leading-edge vortex migrates toward the trailing edge and acts to initiate the trailing-edge vortex after supination. The trailing-edge vortex phenomenon is a wake capture event during stroke reversal – when the wing is translating slowly – so the mechanical work done by the flight motor is very low, and lift efficiency is consequently relatively high at this instant (Fig. 3D, *t1*). Immediately after the wing passes through the vertical alignment, the aerodynamic torque on the wing provided by the captured trailing-edge vortex acts to pitch the wing passively in preparation for the next sweep.

The great benefit of lift mediated by rotational drag is that the aerodynamic force (in contrast to conventional lift from a sweeping wing) is independent of radial position. It is therefore equally effective along the entire wing span, even in the portion of the wing close to the root where velocity due to the sweep of the wing – and hence lift due to translation – is near zero. This feature, in combination with reduced inertial costs during rotation and smaller pitching torques due to reduced moment arm length, is likely to be a key factor in shaping the high aspect ratio wings of mosquitoes. We do not necessarily expect these aerodynamic features to

160 be unique to mosquitoes, but the trailing-edge vortex wake capture mechanism is not a
161 significant feature of fruit fly flight, despite operating at similar Reynolds numbers (Fig. 4B-C). It
162 remains an open question as to why mosquitoes have evolved to operate far outside the usual
163 bounds of kinematic patterns used by other insects. Given that high frequency flapping will
164 undoubtedly incur greater inertial power requirements, one can presume compensatory
165 selective advantages, perhaps in the domain of acoustic communication[19].

166

167

168 Methods

169 **Mosquitoes.** *Culex quinquefasciatus* 'Muheza' strain, originally sourced from the London
170 School of Hygiene and Tropical Medicine, were bred at the University of Sussex and tested at
171 the Royal Veterinary College, London. Groups were maintained in microclimate chambers with
172 controlled humidity (70-75%), temperature (26±2°C) and 12:12 h light cycles. Males between 4
173 and 14 days post-emergence were tested in groups of four to eight individuals.

174 **Kinematics acquisition.** Mosquito wing kinematics were measured using the apparatus
175 illustrated in Extended Data Figure 1a-b, comprised of eight high-speed cameras (Photron SA3:
176 384 × 352 px, Photron Ltd) operating at 10,000 fps with an exposure time of 5μs. Each camera
177 was fitted with a 180 mm macro lenses set at f=16. Consistent backlighting for each camera was
178 provided by a co-axial, high-power infrared LED with divergent and Fresnel lenses to collimate
179 the light in paths of approximately 25 mm diameter. The cameras were arranged such that they
180 viewed a common volume of approximately 20 × 20 × 20 mm at the centre of a transparent flight

arena measuring 330 × 330 × 230 mm. In total, we processed 425 wing beats, over 15 sequences from between 12 and 15 individuals, discernable by their wing length (Extended Data Figure 1c).

Kinematics reconstruction. The eight cameras were calibrated using custom-written, bundle adjustment software running in Matlab (MATLAB, The Mathworks Inc.), which provides estimates of the intrinsic and extrinsic camera parameters, while simultaneously calculating the spatial coordinates of points on a 2D calibration grid in a series of positions and orientations[20].

We selected 15 sequences for kinematic analysis Extended Data Figure 1d), which included all sequences where both wings were visible in seven or more camera views for a minimum of eight wingbeats. Four points on the body were manually registered in three camera views; the base of the proboscis, the tip of the abdomen, and the left and right wing roots. These points were used to calculate the 3D position and orientation of the mosquito body for each frame. A fully automated shape-carving method was used to reconstruct the coordinates of the wing outline[21]. The wing outline was first identified in each camera view using standard image processing tools in Matlab (Fig. 1B). The shape-carving algorithm then identified voxels corresponding to the wing outlines when projected onto each camera plane.

The wingtip position was determined by finding the voxels along the wing outline that were furthest from the wing root. Voxels corresponding to the leading and trailing edges of the wing were then separated using k-means clustering and a cubic spline fitting to each edge from the wing base to the wingtip. The spanwise variation in pitch angle, α, was summarised by regressing the angle between the leading and trailing edge of the wing against spanwise distance along the wing, to give a pitch offset and linear twist gradient.

Computational fluid Dynamics (CFD). The morphological model for CFD analyses was constructed by digitizing the wing outline from microscope images of excised wings and fitting

ellipses to the body in the raw video images. Assuming a low leakiness of hairs at the anterior margin due to the ultra-low Reynolds number[22], we used outlines incorporating the hairs as part of the wing shape. The mean shape of three individuals (Extended Data Figure 10a; red lines) was used for the surface mesh (Extended Data Figure 10b). Uniform thickness was assumed as 1 % of mean chord length with elliptic smoothing at the leading and trailing edges as well as the wing tip and base. The body surface was extracted by manually fitting a series of ellipses to the body in each camera view. Each ellipse was normal to the central axis of the body, which was determined separately using the positions of head and body landmarks. The ellipses were then interpolated by cubic splines and used to generate the mesh surface shown in Extended Data Figure 10c-d.

For our CFD model, we used a dynamic flight simulator[23,24] that is based on the incompressible, unsteady three-dimensional Navier-Stokes equations and can easily integrate the realistic morphology, kinematics and aerodynamics of insect flight. The simulator utilizes a multi-block, overset-grid method in which the computational domain is decomposed into the local grid, clustered near the wings and body, and a global Cartesian grid. The wing and body grids in Extended Data Figure 10e were generated from the surface mesh. The minimum grid spacing from surface is defined based on 0.1/sqrt(Re). The distance between the surface and outer boundary is set to be 2.0 c_m (mean chord lengths) for wing and 1.0 c_m for body grids. The outer boundary conditions for local grids are given by a Cartesian background grid (28R × 14R × 28R; Extended Data Figure 10f). We assumed a symmetric motion of the left and right wings, and applied a symmetric boundary condition at the sagittal plane of the body and background grid. The wing grid was regenerated every time-step after twisting the wing surface, and rotated around wing base. The flapping angles were interpolated by a fifth order Fourier series.

Self-consistency was tested by four CFD cases with coarse, fine and finer grids, and a reduced time-step interval, dt. The time-series data of vertical force, mean aerodynamic force and power are summarized in Extended Data Figure 10g. While there is a slight difference in the coarse case, there is no large discrepancy observed among the other cases. Two time steps (comparing fine and fine dt) also show little difference. Therefore, the grids for fine case with dt=0.01 was used for all subsequent simulations.

Particle Image Velocimetry (PIV). Mosquitoes were placed in the centre of a clear tank (380 × 140 × 300 mm) by a thin wire attached to the dorsal side of the thorax using cyanoacrylate glue. The tank was seeded with a mist of olive oil droplets of approximately 1μm diameter, generated by a compressed air seeding generator (LaVision UK Ltd, UK), and the flow was left for a few minutes to become quiescent. The seeding particles were illuminated using a 10 mJ dual-cavity pulsed laser (Litron LDY-301PIV, ND: YLF, 527 nm, Litron Lasers Ltd, UK). The beam diverged into a sheet of approximately 1mm thickness after passing through a -20 mm cylindrical lens, entering the flight arena from above such that the sheet was parallel with the sagittal plane of the mosquito, incident with the wing half way from root to tip (R = 0.5). Images were captured over a sampling area of 17 × 17 mm around the wing using a single high-speed camera (Photron SA3: 2000 fps, 1024 × 1024 px, Photron Ltd) fitted with a 180 mm macro lens (Tamron) whose axis was normal to the light sheet.

The camera and laser were driven using DAVIS v.7.2.2 software and synchronized by a high-speed controller (LaVision UK, Ltd) operating at a rate of 1000 image pairs per second. The system was post-triggered by a TTL signal and each recording captured 1361 image pairs (limited by camera buffer capacity). The camera was calibrated using a custom calibration plate

(circle diameter ϕ=1 mm; circle separation dx=2 mm) and the calibration procedure in Davis v.7.2.2.

Raw images were pre-processed by subtraction of a sliding background (2 px) and particle intensity normalization (min/max-filter, 10 px) to remove any stationary elements in the images (e.g. reflection from body, legs and antenna). The reflection from the wing is masked manually for presentation. After filtering, the images were cross-correlated to calculate fluid vector fields by multi-path correlation with a decreasing interrogation window size from 64 x 64 (50% overlap) to 16 x 16 (50 % overlap). PIV calculations were performed using Davis v.8.1.5 (LaVision UK, Ltd). Post processing of vector fields involved filling up of empty spaces by interpolation and a 3 x 3 smoothing. We selected the frames before the mosquito began to respond to the laser light (approximately the first 50 frames in a sequence) with relatively low glare on wing.

Blade element model with quasi-steady assumption. In order to highlight the unconventional aerodynamics of hovering mosquitoes, we have compared the forces from the CFD simulations with a blade element model with the quasi-steady assumption that takes into account the translational circulation and drag, and added mass[12,25]. The lift and drag force coefficients, C_L and C_D, were calculated using the mean lift and drag from a separate CFD analysis simulating a spinning mosquito wing model. We used the 3rd cycle (1080°-1170°) to account for the effect of induced downwash from previous strokes. As we found a strong dependency of force coefficients profile on Reynolds number (50-300), C_L and C_D in the blade element model were interpolated by a 2D spline, assuming those as the functions of angle of attack and instantaneous Reynolds number based on mean chord length and instantaneous wing tip velocity. The range of Reynolds number for C_L and C_D covers the maximum instantaneous Reynolds number of *Culex*

mosquitoes, 250, and the C_L and C_D at Re=50 (the 20th percentile of instantaneous Reynolds number) was used if the instantaneous Reynolds number dropped to a value lower than 50.

Data availability statement. Datasets underpinning the current study are available in the Dryad repository [doi:10.5061/dryad.tc29h].

Code availability. The CFD solver[23] and kinematics acquisition code[20,21] are described in further detail elsewhere.

References

1 Simões, P. M. V., Ingham, R. A., Gibson, G. & Russell, I. J. A role for acoustic distortion in novel rapid frequency modulation behaviour in free-flying male mosquitoes. *Journal of Experimental Biology*, doi:10.1242/jeb.135293 (2016).

2 Chin, D. D. & Lentink, D. Flapping wing aerodynamics: from insects to vertebrates. *Journal of Experimental Biology* **219**, 920-932, doi:10.1242/jeb.042317 (2016).

3 Ellington, C. P., van den Berg, C., Willmott, A. P. & Thomas, A. L. R. Leading-edge vortices in insect flight. *Nature* **384**, 626-630 (1996).

4 Somps, C. & Luttges, M. Dragonfly Flight - Novel Uses of Unsteady Separated Flows. *Science* **228**, 1326-1329 (1985).

5 Bomphrey, R. J., Srygley, R. B., Taylor, G. K., Nudds, R. L. & Thomas, A. L. R. Visualising the flow around insect wings. *Phys. Fluids* **14**, S4 (2002).

6 Thomas, A. L. R., Taylor, G. K., Srygley, R. B., Nudds, R. L. & Bomphrey, R. J. Dragonfly flight: free-flight and tethered flow visualizations reveal a diverse array of unsteady lift-generating mechanisms, controlled primarily via angle of attack. *Journal of Experimental Biology* **207**, 4299-4323, doi:10.1242/jeb.01262 (2004).

7 Bomphrey, R. J., Taylor, G. K. & Thomas, A. L. R. Smoke visualization of free-flying bumblebees indicates independent leading-edge vortices on each wing pair. *Experiments in Fluids* **46**, 811-821, doi:10.1007/s00348-009-0631-8 (2009).

8 Srygley, R. B. & Thomas, A. L. R. Unconventional lift-generating mechanisms in free-flying butterflies. *Nature* **420**, 660-664, doi:10.1038/nature01223 (2002).

9 Videler, J. J., Stamhuis, E. J. & Povel, G. D. E. Leading-edge vortex lifts swifts. *Science* **306**, 1960-1962 (2004).

10 Warrick, D. R., Tobalske, B. W. & Powers, D. R. Aerodynamics of the hovering hummingbird. *Nature* **435**, 1094-1097, doi:10.1038/nature03647 (2005).

11 Hedenstrom, A. *et al.* Bat flight generates complex aerodynamic tracks. *Science* **316**, 894-897, doi:10.1126/science.1142281 (2007).

12 Nakata, T., Liu, H. & Bomphrey, R. J. A CFD-informed quasi-steady model of flapping-wing aerodynamics. *J. Fluid Mech.* **783**, 323-343, doi:10.1017/jfm.2015.537 (2015).

13 Whitney, J. P. & Wood, R. J. Aeromechanics of passive rotation in flapping flight. *J. Fluid Mech.* **660**, 197-220, doi:doi:10.1017/S002211201000265X (2010).

14 Ellington, C. P. The aerodynamics of hovering insect flight. V. A vortex theory. *Phil. Trans. R. Soc. Lond. B* **305**, 115-144 (1984).

15 Dickinson, M. H., Lehmann, F.-O. & Sane, S. P. Wing rotation and the aerodynamic basis of insect flight. *Science* **284**, 1954-1960 (1999).

16 Sane, S. P. & Dickinson, M. H. The aerodynamic effects of wing rotation and a revised quasi-steady model of flapping flight. *Journal of Experimental Biology* **205**, 1087-1096 (2002).

17 Aono, H., Liang, F. & Liu, H. Near- and far-field aerodynamics in insect hovering flight: an integrated computational study. *Journal of Experimental Biology* **211**, 239-257, doi:10.1242/jeb.008649 (2008).

18 Fry, S. N., Sayaman, R. & Dickinson, M. H. The aerodynamics of hovering flight in Drosophila. *Journal of Experimental Biology* **208**, 2303-2318, doi:10.1242/jeb.01612 (2005).

19 Cator, L. J., Arthur, B. J., Harrington, L. C. & Hoy, R. R. Harmonic convergence in the love songs of the dengue vector mosquito. *Science* **323**, 1077-1079, doi:10.1126/science.1166541 (2009).

20 Walker, S. M., Thomas, A. L. R. & Taylor, G. K. Photogrammetric reconstruction of high-resolution surface topographies and deformable wing kinematics of tethered locusts and free-flying hoverflies. *Journal of The Royal Society Interface*, doi:10.1098/rsif.2008.0245 (2008).

21 Walker, S. M., Thomas, A. L. R. & Taylor, G. K. Operation of the alula as an indicator of gear change in hoverflies. *Journal of The Royal Society Interface*, doi:10.1098/rsif.2011.0617 (2011).

22 Cheer, A. Y. L. & Koehl, M. A. R. Paddles and rakes - fluid-flow through bristled appendages of small organisms. *J. Theor. Biol.* **129**, 17-39, doi:10.1016/s0022-5193(87)80201-1 (1987).

23 Liu, H. Integrated modeling of insect flight: From morphology, kinematics to aerodynamics. *J. Comput. Phys.* **228**, 439-459, doi:10.1016/j.jcp.2008.09.020 (2009).

24 Nakata, T. & Liu, H. A fluid-structure interaction model of insect flight with flexible wings. *J. Comput. Phys.* **231**, 1822-1847, doi:10.1016/j.jcp.2011.11.005 (2012).

25 Berman, G. J. & Wang, Z. J. Energy-minimizing kinematics in hovering insect flight. *J. Fluid Mech.* **582**, 153-168, doi:10.1017/s0022112007006209 (2007).

26 Altshuler, D. L., Dickson, W. B., Vance, J. T., Roberts, S. P. & Dickinson, M. H. Short-amplitude high-frequency wing strokes determine the aerodynamics of honeybee flight. *Proc. Natl. Acad. Sci. U. S. A.* **102**, 18213-18218, doi:10.1073/pnas.0506590102 (2005).

27 Willmott, A. P. & Ellington, C. P. The mechanics of flight in the hawkmoth Manduca sexta I. Kinematics of hovering and forward flight. *Journal of Experimental Biology* **200**, 2705-2722 (1997).

28 Vance, J. T. & Roberts, S. P. The effects of artificial wing wear on the flight capacity of the honey bee Apis mellifera. *Journal of Insect Physiology* **65**, 27-36, doi:http://dx.doi.org/10.1016/j.jinsphys.2014.04.003 (2014).

29 Phillips, N., Knowles, K. & Bomphrey, R. J. The effect of aspect ratio on the leading-edge vortex over an insect-like flapping wing. *Bioinspiration & Biomimetics* **10**, 056020 (2015).

Acknowledgments

The authors were supported by the EPSRC (EP/H004025/1), BBSRC (BB/J001244/1). RJB was supported by an EPSRC Career Acceleration Fellowship. SMW was supported by a Royal Society University Research Fellowship. The work reported in this paper was funded by the Autonomous Systems Underpinning Research (ASUR) programme under the auspices of the Defence Science and Technology Laboratory (Dstl), UK Ministry of Defence. The authors acknowledge useful discussions with Prof. I. Russell and Dr G. Gibson, Dr P. Simoes for rearing the mosquitoes, and Ms F Albert-Davie and Ms M. Inglis for assistance during raw data collection. The authors thank Prof. G. Taylor for the loan of four high-speed cameras purchased on European Research Council (ERC) grant 204513, and Prof. H. Liu for the permission to use the simulator and surface pressure distribution of the fruit fly wing.

Author Contributions

RJB and SMW conceived the experimental design; NP & SMW designed and constructed the apparatus and NP led the data collection; all authors contributed to data collection; SMW processed the raw data to extract detailed kinematics; TN performed the CFD simulations; NP, TN and RJB collected and processed the PIV data; RJB drafted the manuscript; all authors contributed to data interpretation and manuscript preparation.

Author Information

Reprints and permissions information is available at www.nature.com/reprints. The authors have no competing financial interests. Correspondence and requests for materials should be addressed to rbomphrey@rvc.ac.uk.

Figure 1. Low-amplitude mosquito kinematics. **a**, three axes and angles that define flapping wing kinematics; stroke position, φ (within the stroke plane, pink), wing pitch angle, α, deviation angle, θ. **b**, eight views of a *C. quinquefasciatus* mosquito, showing automated extraction of wing outlines. **c**, standardized stroke cycle kinematics from one individual (mean±s.d.; *n*=33 wingbeats). Pitch angle, α, is shown for the base and tip of the wing to highlight longitudinal twist and pitching rotations that are important for unsteady aerodynamics. **d**, dorsal (top) and lateral (bottom) views of characteristic motions (*R*=0.75 wing length) for, left-to-right, mosquito, fruit fly[18], honeybee[26] and hawkmoth[27]. Reynolds numbers (based on mean tip velocity and mean chord length) and aspect ratios for each insect are given[18,23,28].

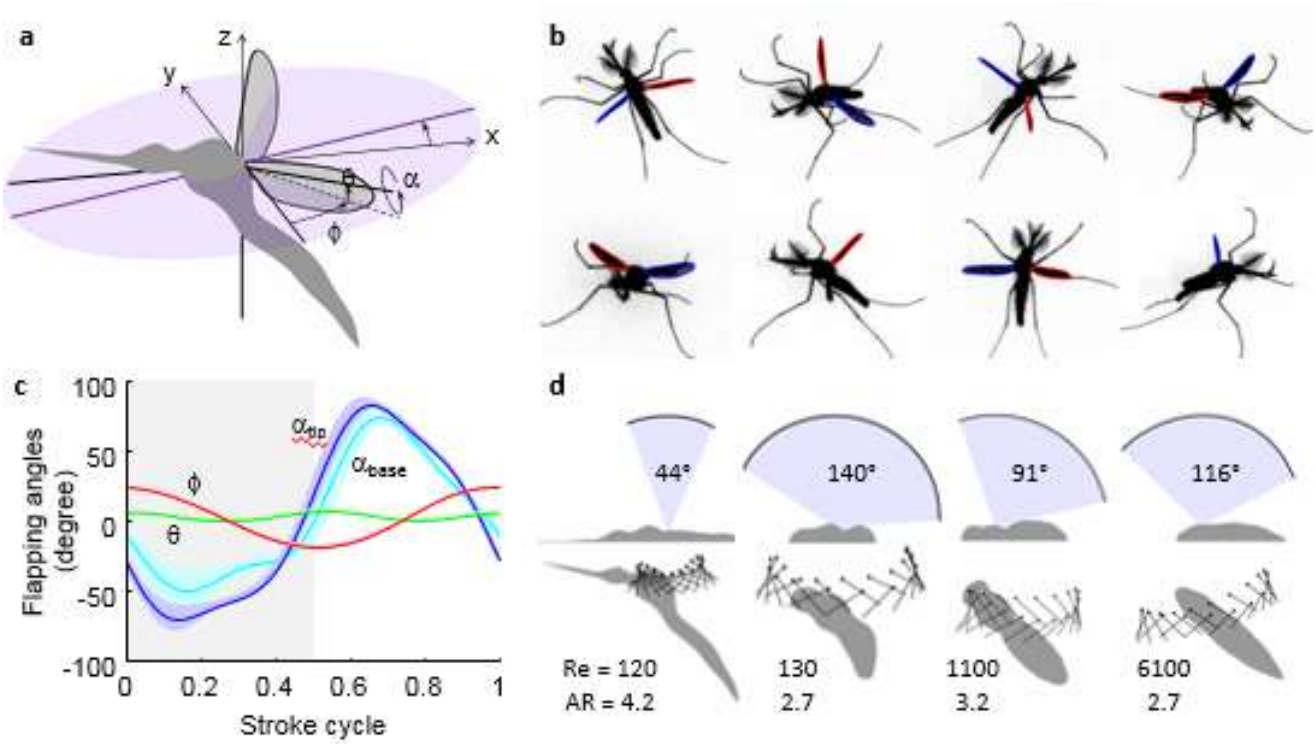

Figure 2. Validation of CFD (**a)** with PIV (**b**) quantitative flow fields. Left-to-right: End of pronation (t/T = 0.22), late downstroke (t/T = 0.36), end of supination (t/T = 0.70) and late upstroke (t/T = 0.84); green shading shows areas of no data. Red and blue patches show clockwise and anticlockwise vorticity. Flow velocity field planes are shown at R = 0.5 wing length for both CFD and PIV.

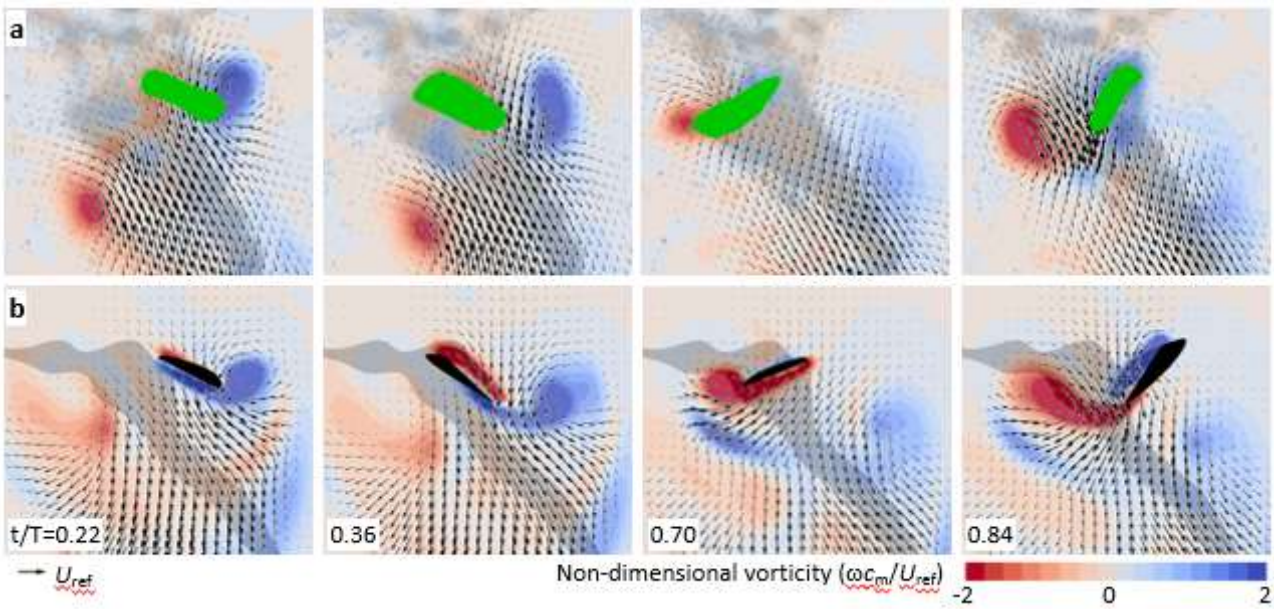

Figure 3. Aerodynamic forces generated by the wings and the mechanisms that produce them: trailing-edge vortices, leading-edge vortices and rotational drag. **a**, single-wing total aerodynamic force (red), lift (black), drag (blue) and side-force (green). **b**, lift from CFD (black) compared against a simple quasi-steady model (grey). Orange shading shows where the quasi-steady model over-predicts the force estimate from the CFD simulation, whereas green shows under-prediction. **c**, partitioning of the lift force (black) into the portion derived from the integrated pressure on the anterior half of the wing (purple), the posterior half (cyan), and the viscous contribution (dashed). Note the fluctuating contributions during the downstroke (t/T = 0-0.5). **d**, aerodynamic power. **e**, the effect of increasing wing stroke amplitude (see insert for range) while maintaining mean wing tip velocity is to reduce the relative contribution to lift attributable to unsteady effects. **f-j**, surface pressure at *t1-t5* on the wing (blue to red shading). Overlain are instantaneous streamlines (grey) and flow velocity vectors (black arrows) for selected vertical slices through the three-dimensional flow field at planes 0.6R or 0.75R from

wing base. Body (dashed line) and wing outlines (solid line, leading edge in bold) are shown for orientation.

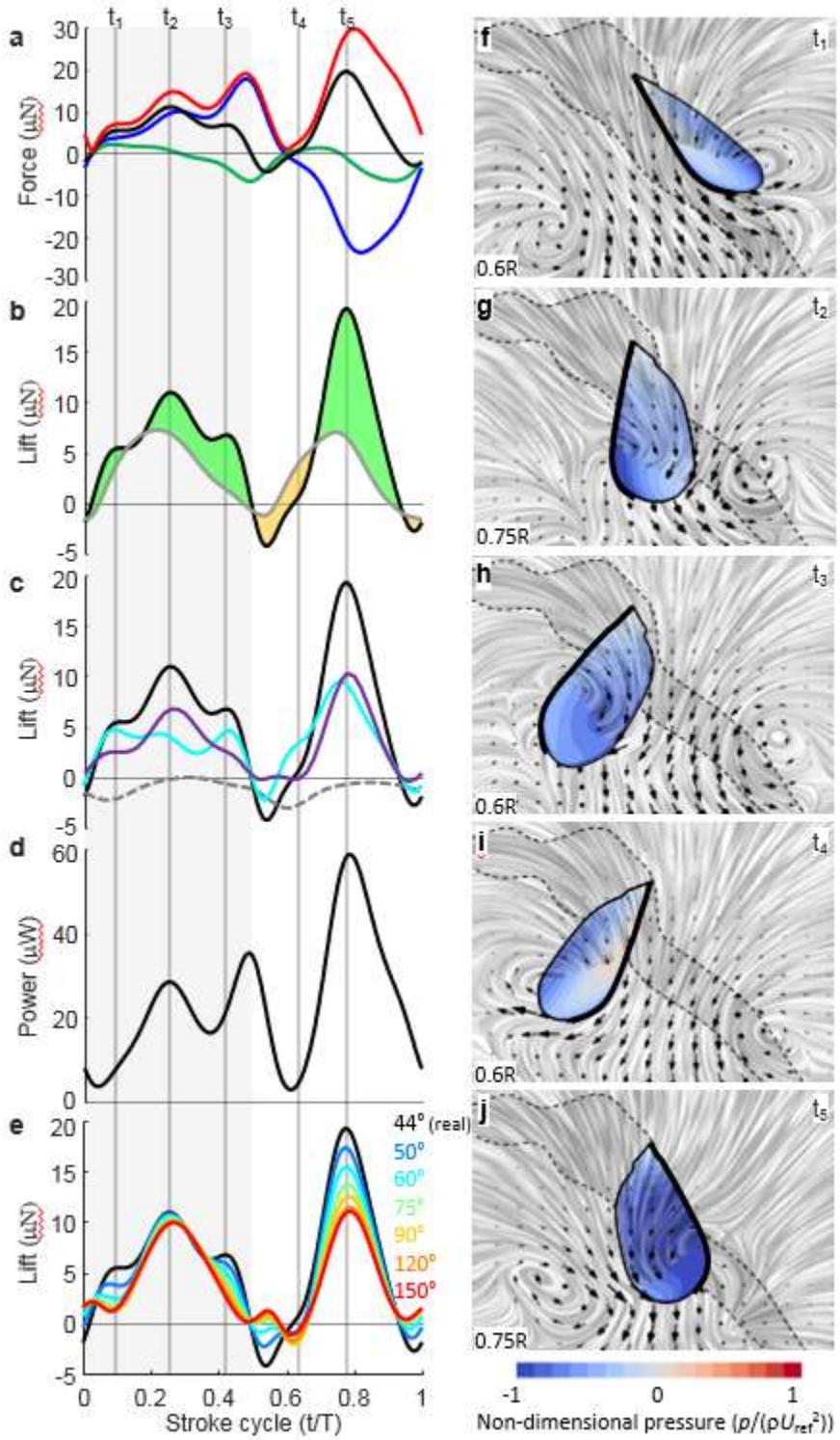

Figure 4. Wing pronation. **a**, the end of each half stroke in mosquitoes is characterized by a shift in the rotational axis (green dot) from leading to trailing edge. Black arrows indicate local motion of the wing during pronation (at 0.75R, indicated in top row); red arrows indicate the resultant aerodynamic force vector (depicted at the chord-wise centre of pressure). Despite rapid pitching down at t/T=0.10 and faster motion of the leading edge, the trailing edge remains almost stationary yet generates the majority of the lift at this instant due to the formation of a trailing edge vortex caused by the induced flow from the preceding upstroke. Pressure distributions (shaded blue to red) on the upper surface of the mosquito (**b**) and fruit fly (**c**) at five moments through the downstroke. Red arrows in (**b**) show the signature of the trailing-edge vortex, visualised by a region of intense low pressure along the trailing portion of the wing, which is not present on the fruit fly wing (**c**). Later in the downstroke, a low pressure region from the leading-edge vortex starts outboard and grows towards the wing root, as described elsewhere[29] for both species (green arrow).

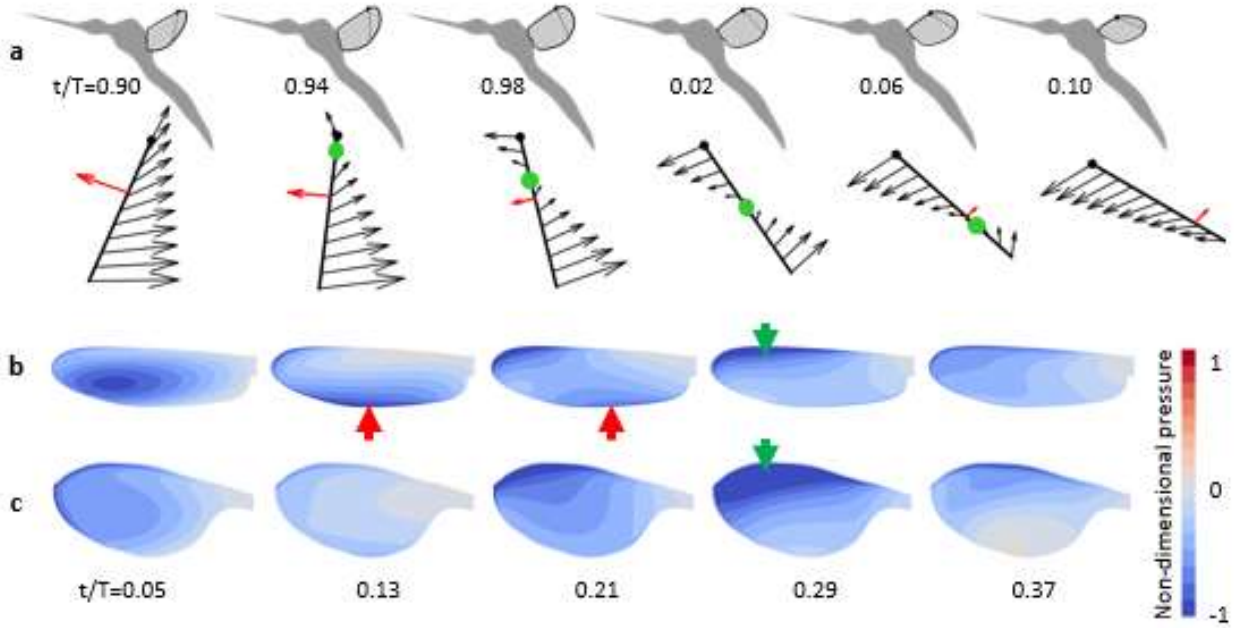

423 Extended Data Figures

424 **Extended Data Figure 1.** Mosquito kinematics acquisition rig, wing lengths and mean
425 kinematic patterns. **a**, CAD representation and **b**, photograph of the apparatus used to record the
426 body motion and wing kinematics of mosquitoes. The recording volume lies at the intersection of
427 the fields of view of eight high-speed cameras, each creating a silhouette image of the mosquito
428 by the shadow from high power IR-LED illumination. **c**, wing length estimates for mosquitoes
429 captured in each of 15 sequences (M01-M15). Each estimate shows the median as a black line
430 with shading representing the 95% confidence interval based upon all wing beats from each
431 sequence. Green and purple boxes group sequences that could not be reliably separated using
432 Tukey's Honestly Significant Difference criterion, although they may come from different
433 individuals of very similar size. As such, our fully-processed dataset of 15 sequences comprises
434 between 12 and 15 individual mosquitoes. **d**, mean wing beat kinematics for all wingbeats in
435 each of 15 recorded sequences. With reference to **c**, M01, M06 and M09, coloured green, may be
436 from the same individual. Similarly, M05 and M11 may also be from a single individual.
437

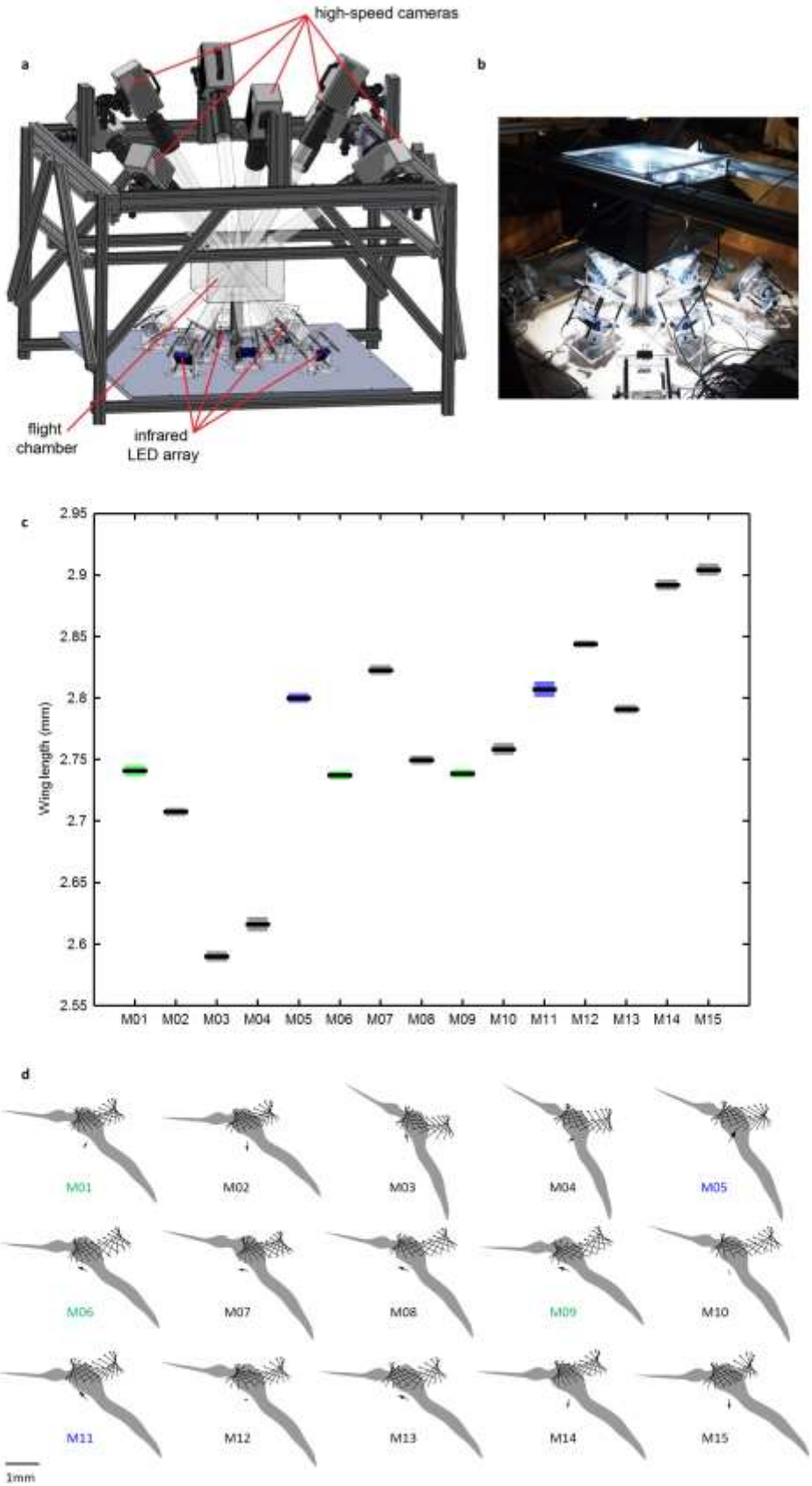
a
high-speed cameras
flight chamber
infrared LED array
b
c
Wing length (mm)
2.95
2.9
2.85
2.8
2.75
2.7
2.65
2.6
2.55
M01 M02 M03 M04 M05 M06 M07 M08 M09 M10 M11 M12 M13 M14 M15
d
M01 M02 M03 M04 M05
M06 M07 M08 M09 M10
M11 M12 M13 M14 M15
1mm

Extended Data Figure 2. Wing surface pressure distribution and fluid flow visualised by streamlines showing consistency across each of the 15 mosquito sequences. Each image corresponds to key instant *t1*. Formation of the trailing-edge vortex due to capture of the induced flow from the preceding upstroke causes a distinct region of low pressure on the posterior portion of the wing.

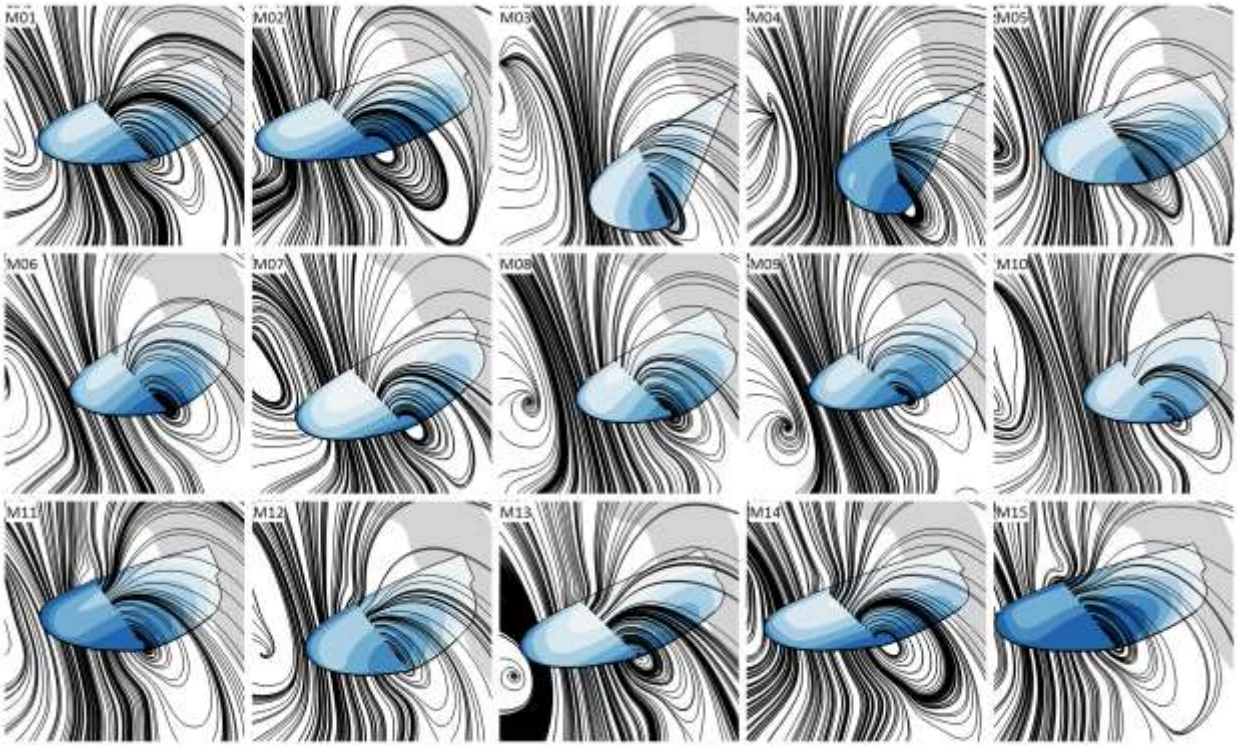

Extended Data Figure 3. Wing surface pressure distribution and fluid flow visualised by streamlines showing consistency across each of the 15 mosquito sequences. Each image corresponds to key instant *t2*. The downstroke force peak is dominated by a leading-edge vortex and corresponding low pressure on the anterior portion of the wing. The trailing-edge vortex has usually shed by this point in the stroke cycle.

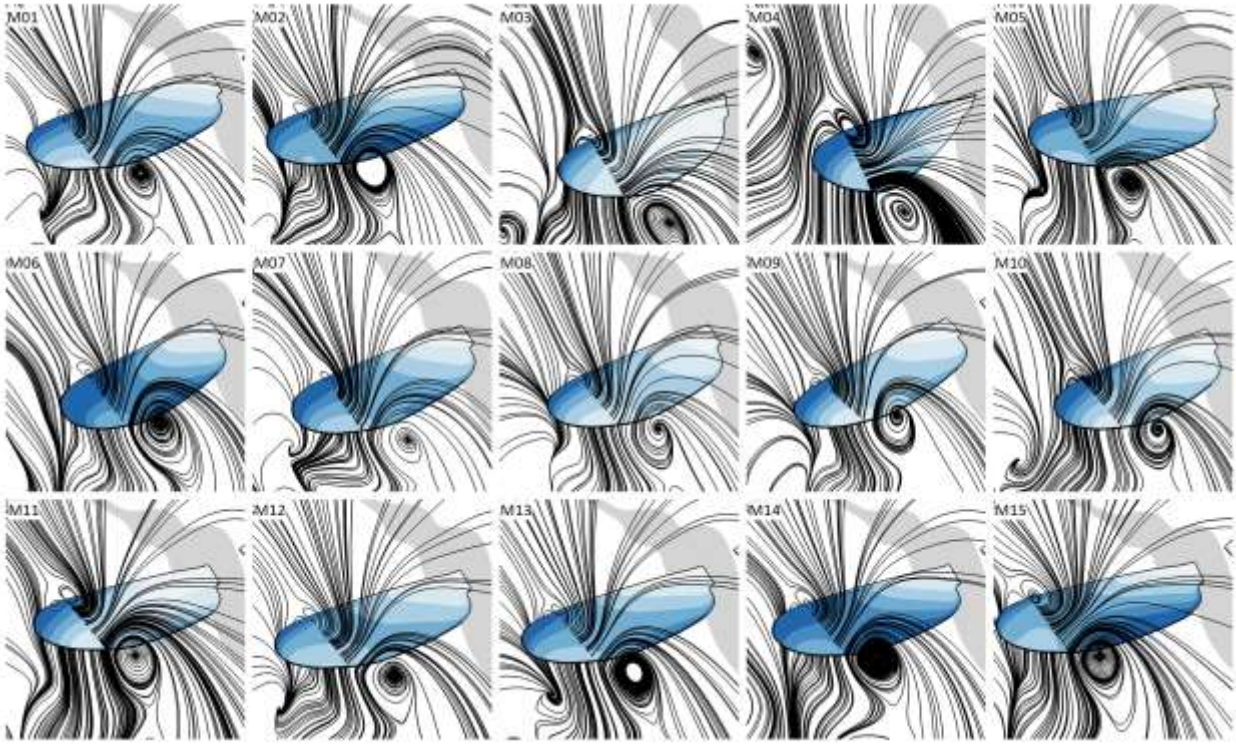

Extended Data Figure 4. Wing surface pressure distribution and fluid flow visualised by streamlines showing consistency across each of the 15 mosquito sequences. Each image corresponds to key instant *t3*. A low pressure region is evident on the posterior portion of the wing due to lift from rotational drag as the wing rotates around an axis close to the leading edge.

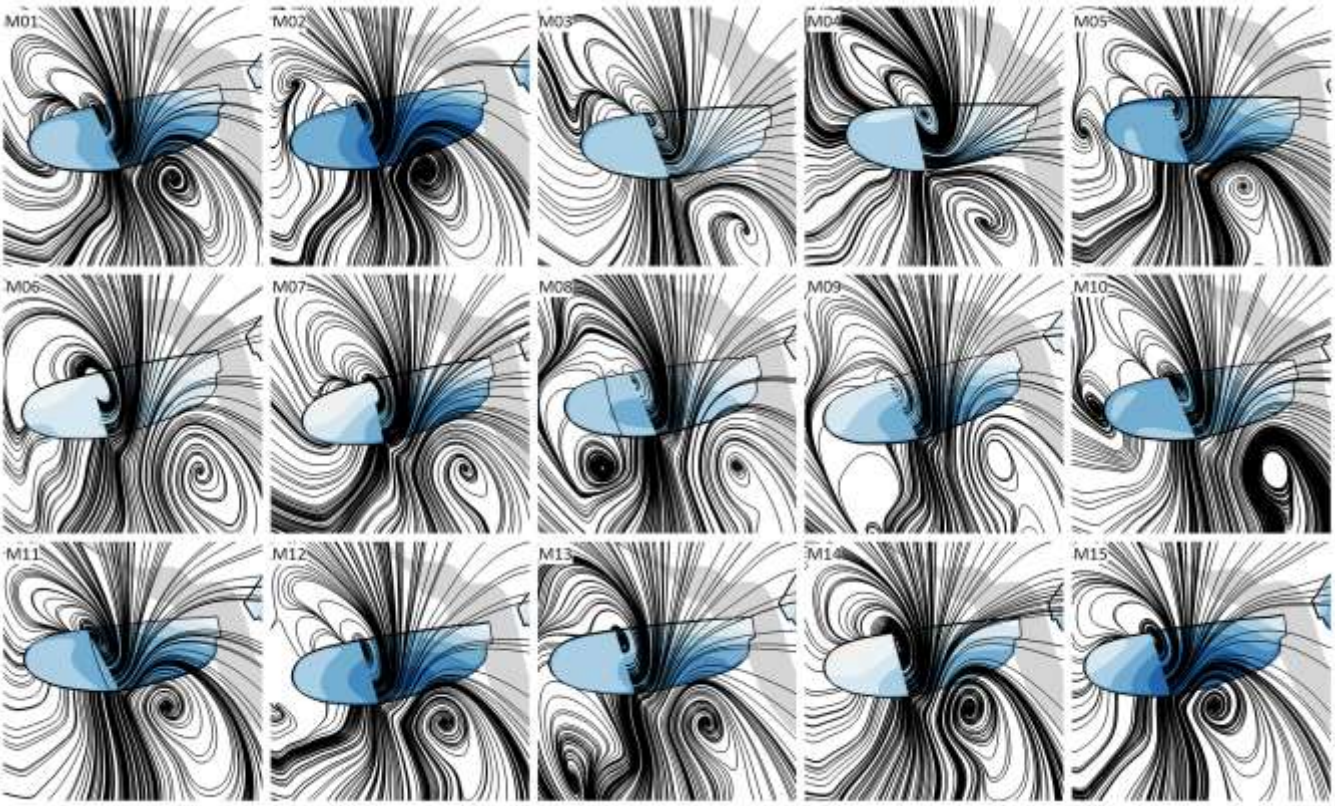

Extended Data Figure 5. Wing surface pressure distribution and fluid flow visualised by streamlines showing consistency across each of the 15 mosquito sequences. Each image corresponds to key instant *t4*. Formation of a trailing-edge vortex on the aerodynamic upper, (anatomical ventral) surface of the wing during the upstroke due to capture of the induced flow from the preceding downstroke causes a distinct region of low pressure on the posterior portion of the wing.

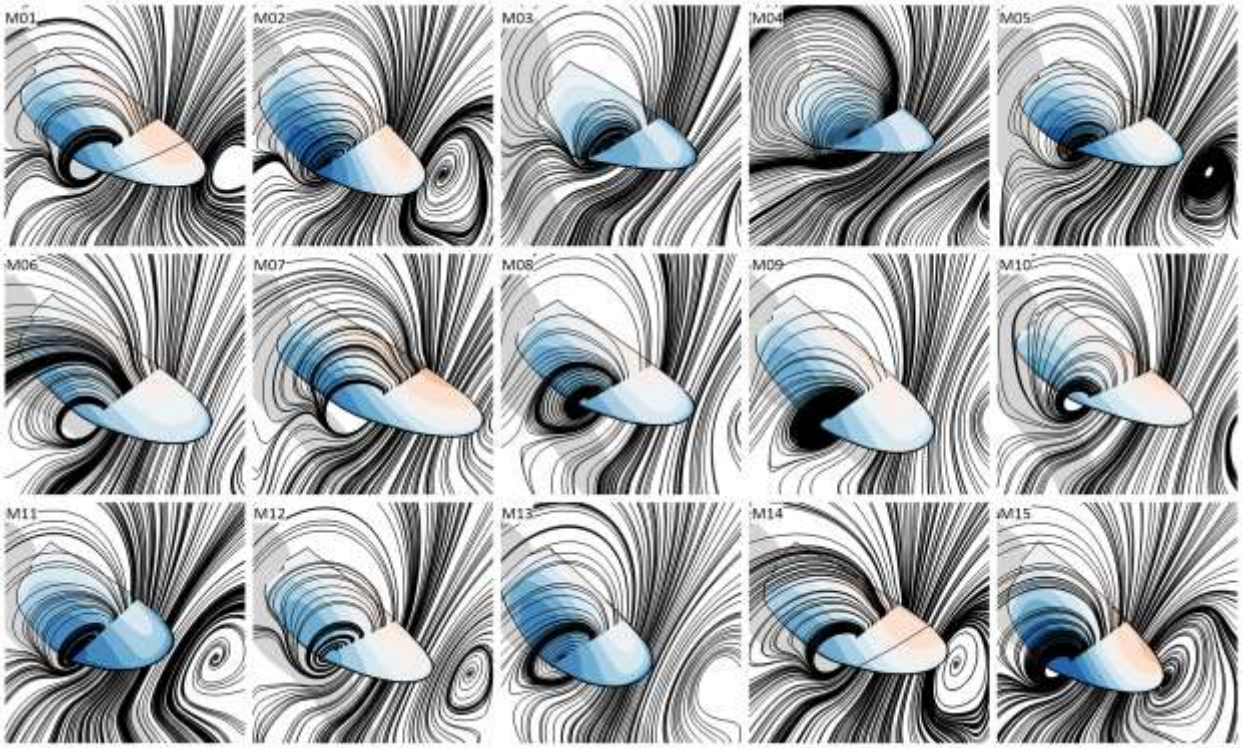

Extended Data Figure 6. Wing surface pressure distribution and fluid flow visualised by streamlines showing consistency across each of the 15 mosquito sequences. Each image corresponds to key instant *t5*. A low pressure region exists over much of the aerodynamic upper, (anatomical ventral) surface of the wing as the result of a combination of rotational drag (caused by wing rotation around an axis close to the leading edge) and the remnants of the upstroke's leading-edge vortex (which is no longer coherent in most examples but is retained in M03, M04, M06, M08, M11).

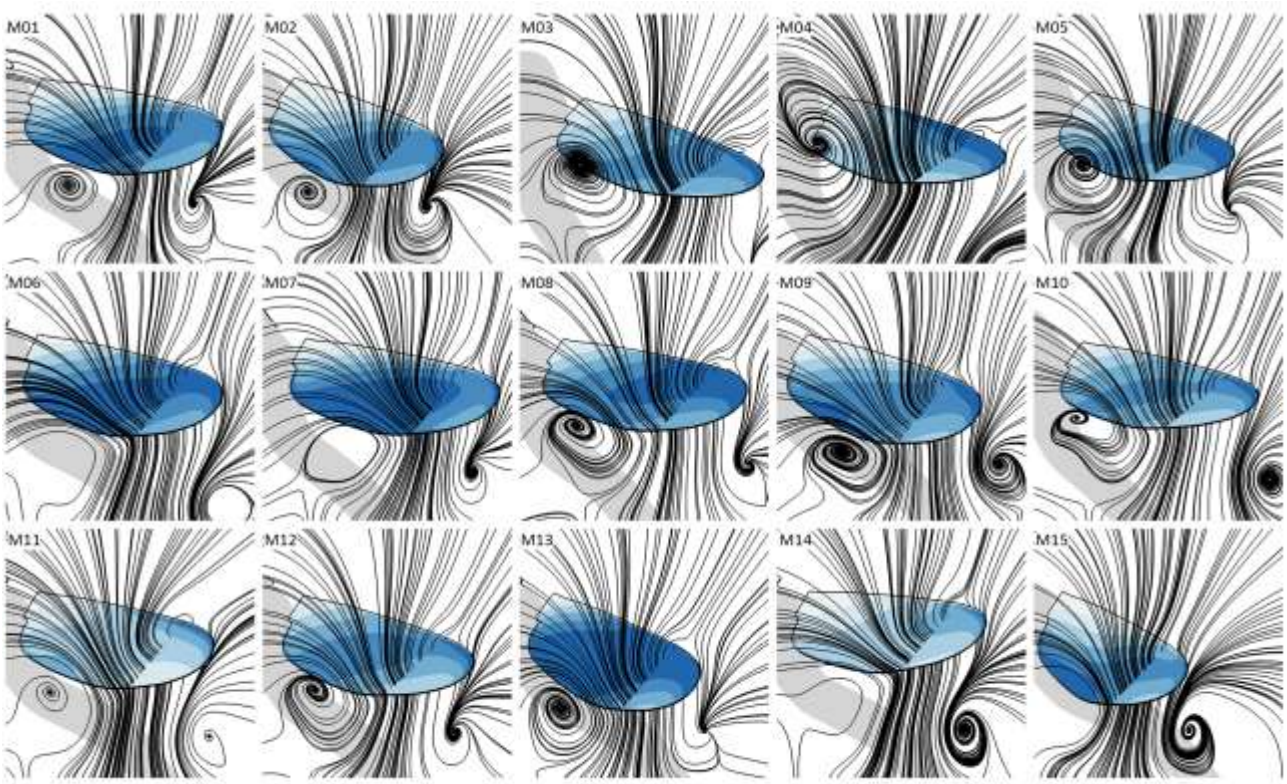

t5. Leading-edge vortex and rotational drag (upstroke)

Extended Data Figure 7. Comparison of the local flow conditions at the trailing edge of the wings of mosquitoes and fruit flies during pronation (t/T=0.09). The comparatively higher local angle of attack at the mosquito is caused by the induced flow from the preceding upstroke. This is a product of kinematic tuning and a form of wake capture that leads to roll up of a transient, coherent, trailing-edge vortex. The vortex contributes to weight support along much of the length of the slender mosquito wing, despite it having little ground velocity during the rotational phase of the stroke cycle.

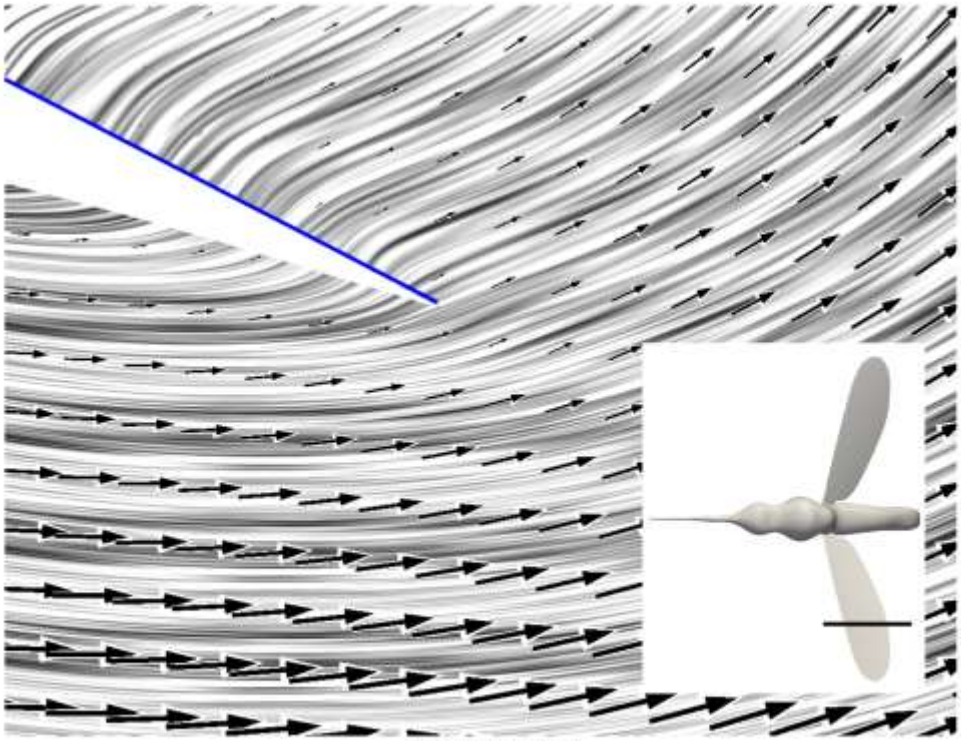

Mosquito (t/T=0.09)

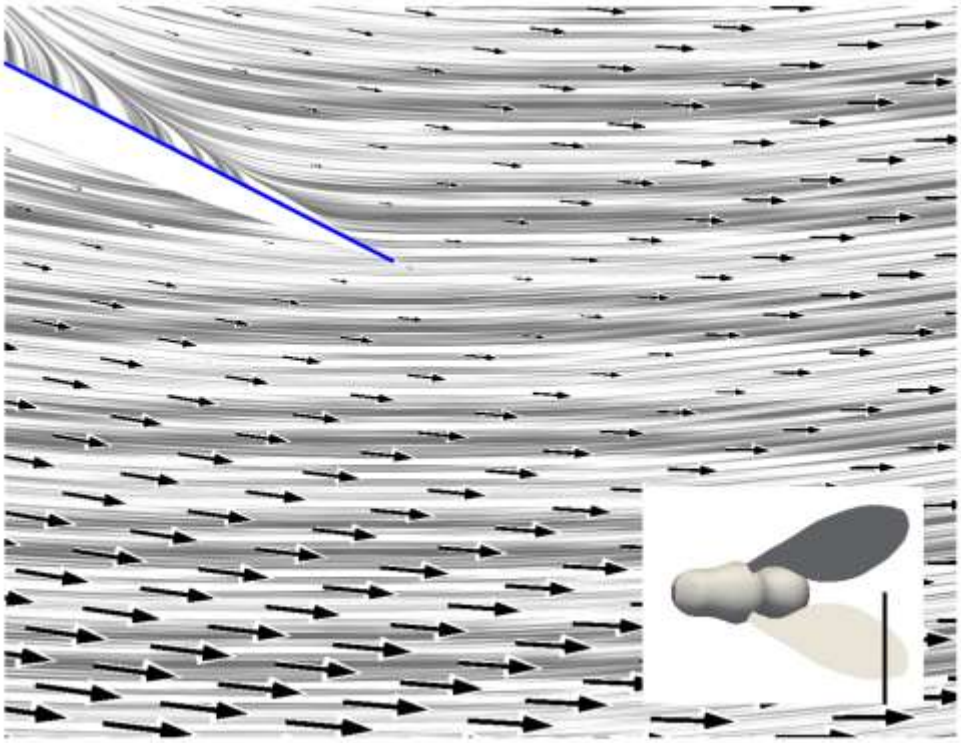

Fruit fly (t/T=0.09)

Extended Data Figure 8. Comparison of computed CFD lift force (black) compared against a simple quasi-steady model (grey) for each of 15 mosquito flight sequences. Orange shading shows where the quasi-steady model over-predicts the force estimate from the CFD simulation, whereas green shows under-prediction. (See also Fig. 3)

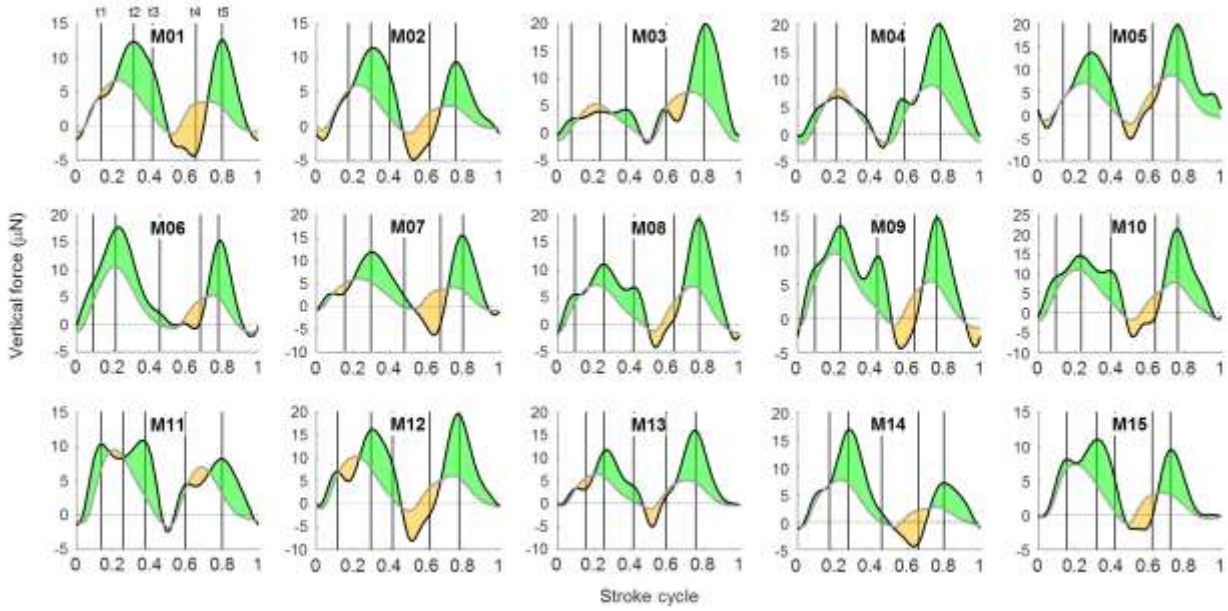

Extended Data Figure 9. Lift and drag polars from high-fidelity CFD simulations of the mosquito wing model in continuous rotational sweep at four Reynolds numbers. These were used to create dynamic lift coefficients for the blade element modelling with quasi-steady assumption. Coefficients are calculated for the third rotation, to account for the reduction in effective angle of attack when wings operate in the induced downwash from the preceding wing stroke.

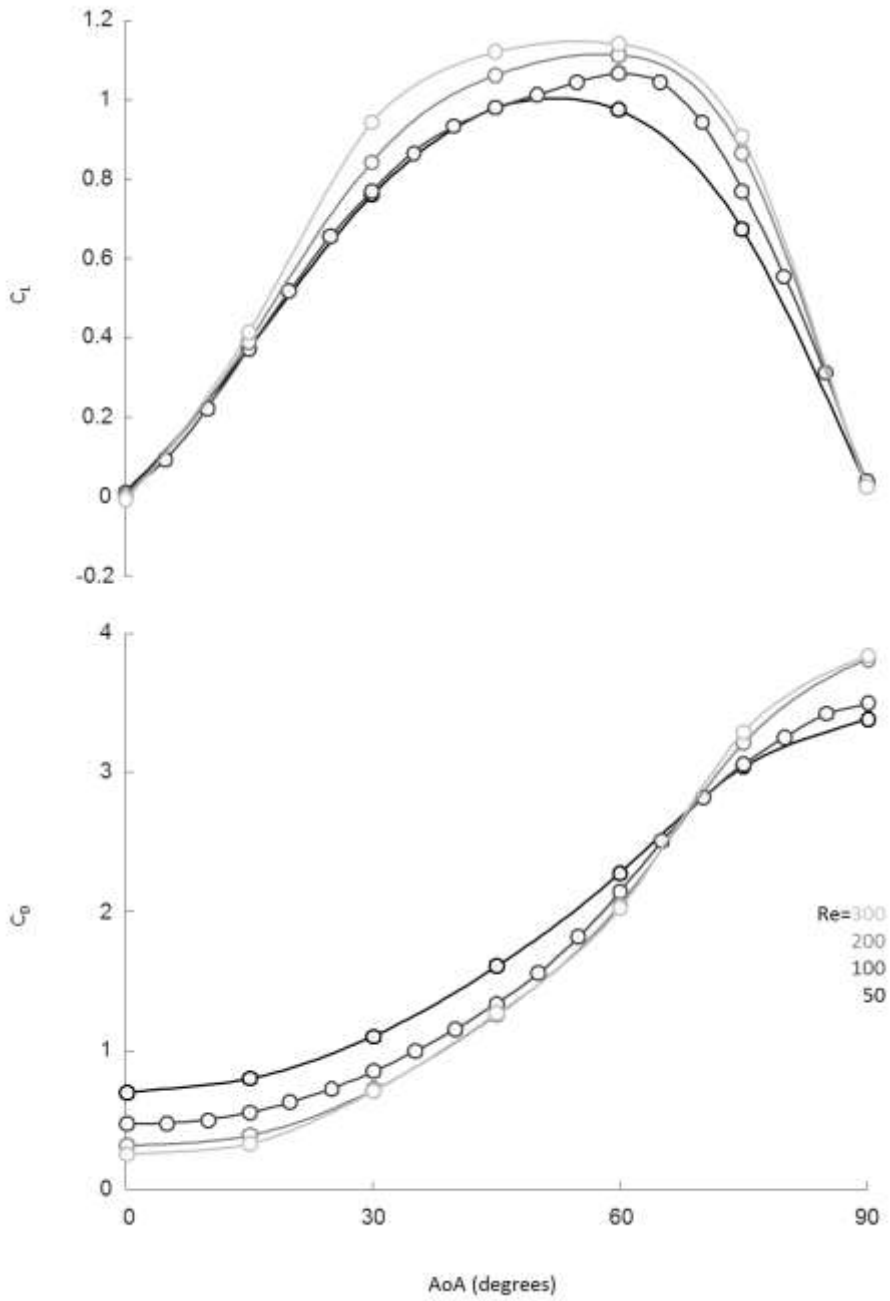

498 **Extended Data Figure 10.** Morphology extraction (**a**, **c**) and the CFD grid used for simulations
499 (**b**, **d-f**). We used the mean wing planform of three mosquitoes, extracted from microscope
500 images of recently excised wings, to generate the wing grids used in our CFD simulations. The
501 body shape was approximated from the silhouettes in the raw video data by fitting ellipses
502 normal to the central axis of the body taken from each of the eight camera views. **g,** CFD grid
503 and time-step independence was verified after performing simulations with variable cell density
504 and time-step intervals.

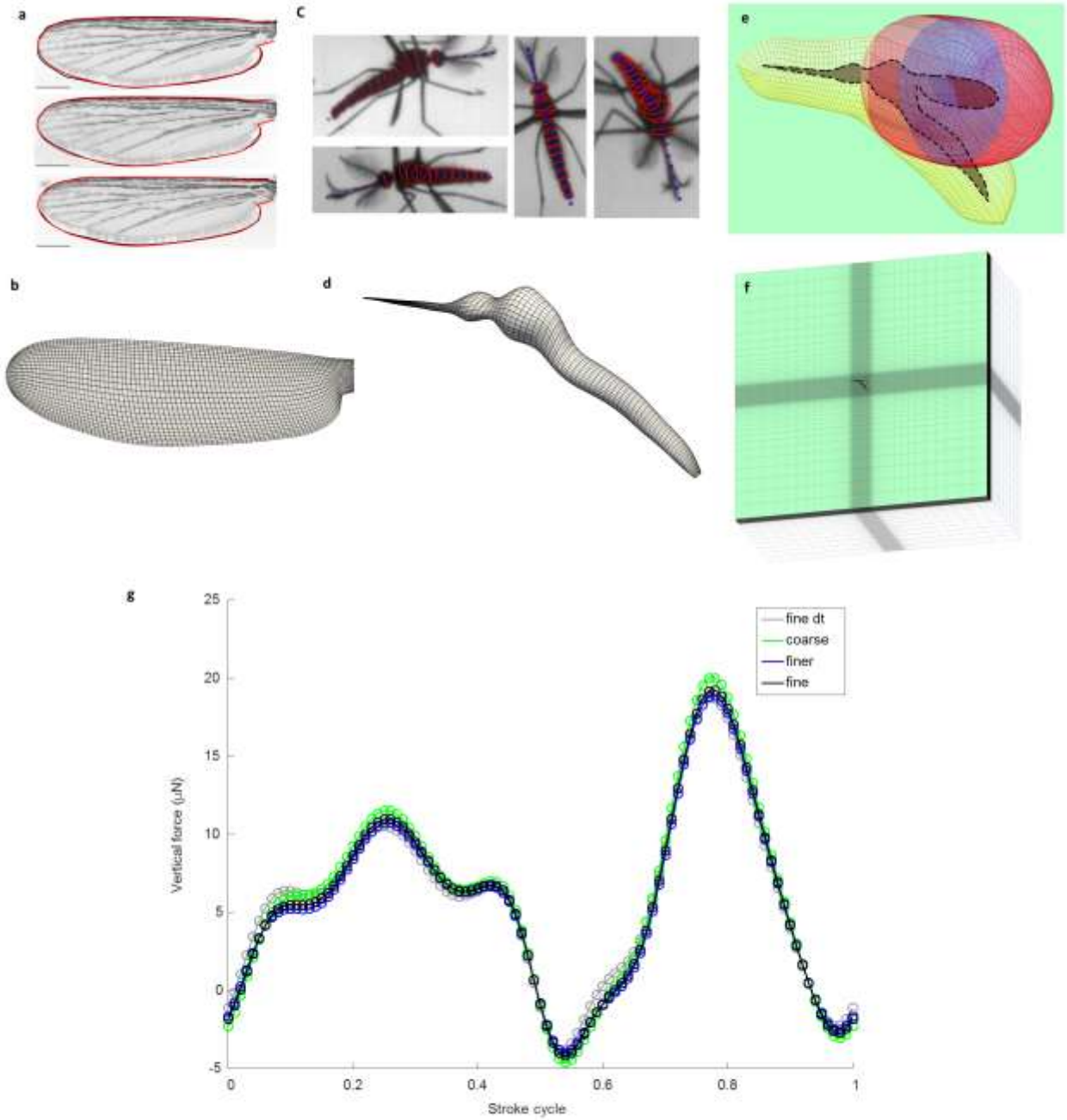

	grid (wing)	grid (body)	grid (background)	time step	Mean vertical force (mN)	Mean aerodynamic power (mW)
finer	71x121x51	41x111x31	188x108x201	0.01	5.69 (-1.95)	22.72 (-2.25)
fine	51x101x41	33x91x21	141x81x151	0.01	5.80 (0.00)	23.24 (0.00)
coarse	31x81x31	21x71x15	94x54x101	0.01	6.06 (4.47)	24.46 (5.25)
fine dt	51x101x41	33x91x21	141x81x151	0.005	5.91 (1.79)	22.99 (-1.10)

Supplementary Video. Video showing: *i)* the experimental apparatus, *ii)* raw data, *iii)* wing geometry routine, *iv)* kinematics, *v)* vortex wake (using isosurfaces of the Q-criterion), and *vi)* pressure distribution and instantaneous flow fields at key instants (*t1-t5*) throughout the wing stroke cycle.

Available via Nature online:

https://www.nature.com/nature/journal/v544/n7648/fig_tab/nature21727_SV1.html